Understanding the Role of Hydroxyl Functionalization in Linear Poly(ethylenimine) for Oxidation-Resistant Direct Air Capture of CO_2

Anthony J. Varni,[a] Lucas S. Thigpen,[a] Marcos F. Calegari Andrade,[a] Maxwell A. T. Marple,[a] Elwin Hunter-Sellars,[a] Amitesh Maiti,[a] Sichi Li,*[a] Simon H. Pang*[a]

[a] Materials Science Division
Lawrence Livermore National Laboratory
7000 East Avenue, Livermore, CA 94550
E-mail: li77@llnl.gov, pang6@llnl.gov

Abstract: Aminopolymer-based adsorbents are a prominent class of materials being used for direct air capture of CO_2 at the industrial scale. However, improving their working lifetime, specifically by increasing their resilience to oxidative degradation, remains an ongoing challenge. Towards this end, functionalization of aminopolymers with non-amine functionalities such as hydroxyls has emerged in recent years as a promising strategy towards improving adsorbent lifetime. Although there is a growing body of work demonstrating the effectiveness of this approach and investigating the origin of this improved stability, studies to date have primarily focused on branched aminopolymer systems such as branched poly(ethylenimine). In this work, we use hydroxyl-functionalized linear poly(ethylenimine) to continue to probe the underlying protective mechanism of this strategy. A combination of thermogravimetric analysis, NMR relaxometry, differential scanning calorimetry, and computational simulations is used to better understand the relationship between extent of chemical functionalization, physical properties, and adsorbent performance.

Introduction

Solid-supported aminopolymer adsorbents are one of the leading technologies being implemented for direct air capture (DAC) of CO_2 at the pilot scale.[1–4] However, one of the primary challenges associated with this class of materials is their tendency to degrade over repeated process cycling, particularly in the presence of oxygen and elevated temperatures.[5–15] In recent years, incorporation of non-amine functional groups, most commonly hydroxyls, into the polymer structure (Figure 1) has gained increasing attention as a strategy towards increasing the oxidative stability of the aminopolymer based sorbents,[16–26] allowing for extended working lifetimes under relevant operating conditions. One potential explanation for this improved stability is the decreased polymer mobility due to increased persistence of hydrogen bonds, as reported by Li et al.,[27] and while this approach has been demonstrated/explored in branched poly(ethylenimine) (branched PEI or BPEI) systems,[16–23] as well as small oligoamines such as tetraethylenepentamine (TEPA)[24,25] and pentaethylenehexamine (PEHA),[26] it has not yet been applied to linear polyamines such as linear poly(ethylenimine) (linear PEI or LPEI). Continuing to explore this phenomenon and determining whether this functionalization strategy imparts a similar benefit to linear polymer systems is beneficial with respect to the design of future materials as well as solidifying a fundamental understanding of the observed performance.

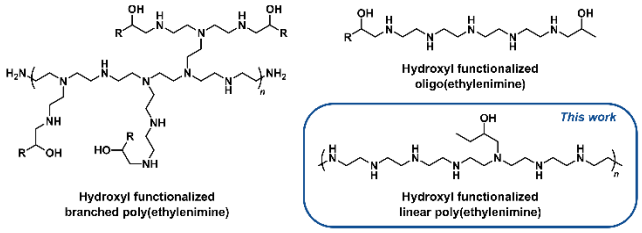

Figure 1. Representative structures of hydroxyl-functionalized aminopolymers and oligomers investigated to date and the hydroxyl-functionalized linear poly(ethylenimine) system reported in this work.

In this report, we investigate the effect of varying levels of hydroxyl content in linear poly(ethylenimine). Hydroxyl-functionalized LPEIs were synthesized via reaction with 1,2-epoxybutane (EB-LPEIs) to have 3.8%, 6.5%, 12.5%, and 17.5% of the amine functionalities containing a tethered hydroxyl group. The CO_2 uptake performance of these materials, supported on mesoporous silica (SBA-15), was investigated via thermogravimetric analysis (TGA) under dry DAC conditions as a function of oxidation time, which highlighted that the hydroxyl moieties generally have a similar protective effect to that observed in BPEI systems. The sorbents were characterized via differential scanning calorimetry (DSC) and solid-state nuclear magnetic resonance (NMR) relaxometry to establish a correlation between the sorbent's physical properties and the resulting performance (e.g. oxidative stability). Finally, computational investigations were used to help identify the role of hydroxyl groups in these LPEI systems.

Results and Discussion

Synthesis and Characterization of EB-LPEI Sorbents

Commercially available linear poly(ethylenimine) (M_n = 2500 g/mol) was treated with varying amounts of 1,2-epoxybutane to produce a series of LPEIs with varying hydroxyl content (Figure 2A), the degree of which was calculated via ^{1}H NMR (Figure 2B, full ^{1}H and ^{13}C NMR spectra are shown in Figures S1-S8). The resulting series had either 3.8%, 6.5%, 12.5%, or 17.5% of the repeat units functionalized with pendant hydroxyl groups via ring opening reaction with the epoxide species, corresponding to an average of approximately 2.2, 3.8, 7.3, and 10.2 hydroxyl groups per polymer chain. LPEI and the series of EB-LPEIs were then used to prepare composites with SBA-15 via wet impregnation at polymer loadings of 40 weight percent relative to total sorbent mass.

CO_2 Uptake and Oxidative Stability

CO_2 uptake capacities for the series of 40 wt% (EB-)LPEI/SBA-15 sorbents were evaluated via thermogravimetric analysis (TGA) using dry 410 ppm CO_2 in N_2. As shown in Figure 2C, relative to unfunctionalized LPEI's capacity of 0.065 mmol CO_2 per mmol N (0.61 mmol CO_2 per gram sorbent), uptake capacities were observed to decrease slightly for 3.8% EB-LPEI and 6.5% EB-LPEI, which had values of 0.060 and 0.054 mmol CO_2 per mmol N (0.53 and 0.46 mmol CO_2 per gram sorbent), respectively. While these values are relatively low compared to those observed for branched poly(ethylenimine) (~0.15 mmol

CO_2 per mmol N),[28] they are in a similar range to other reported values for LPEI at similar loadings.[29] Interestingly, the higher functionalization extents of 12.5% and 17.5% resulted in dramatically lower uptake values, both of which were around 0.035 mmol CO_2 per mmol N. The general decrease in uptake capacities can be at least partially attributed to the increasing proportion of less reactive tertiary amines in the sorbent as hydroxyl content increases, although the origins of the relatively large drop in capacity moving from 6.5% to 12.5% is unclear. Finally, uptake kinetics were evaluated for the polymer series (Figures S10-S11).

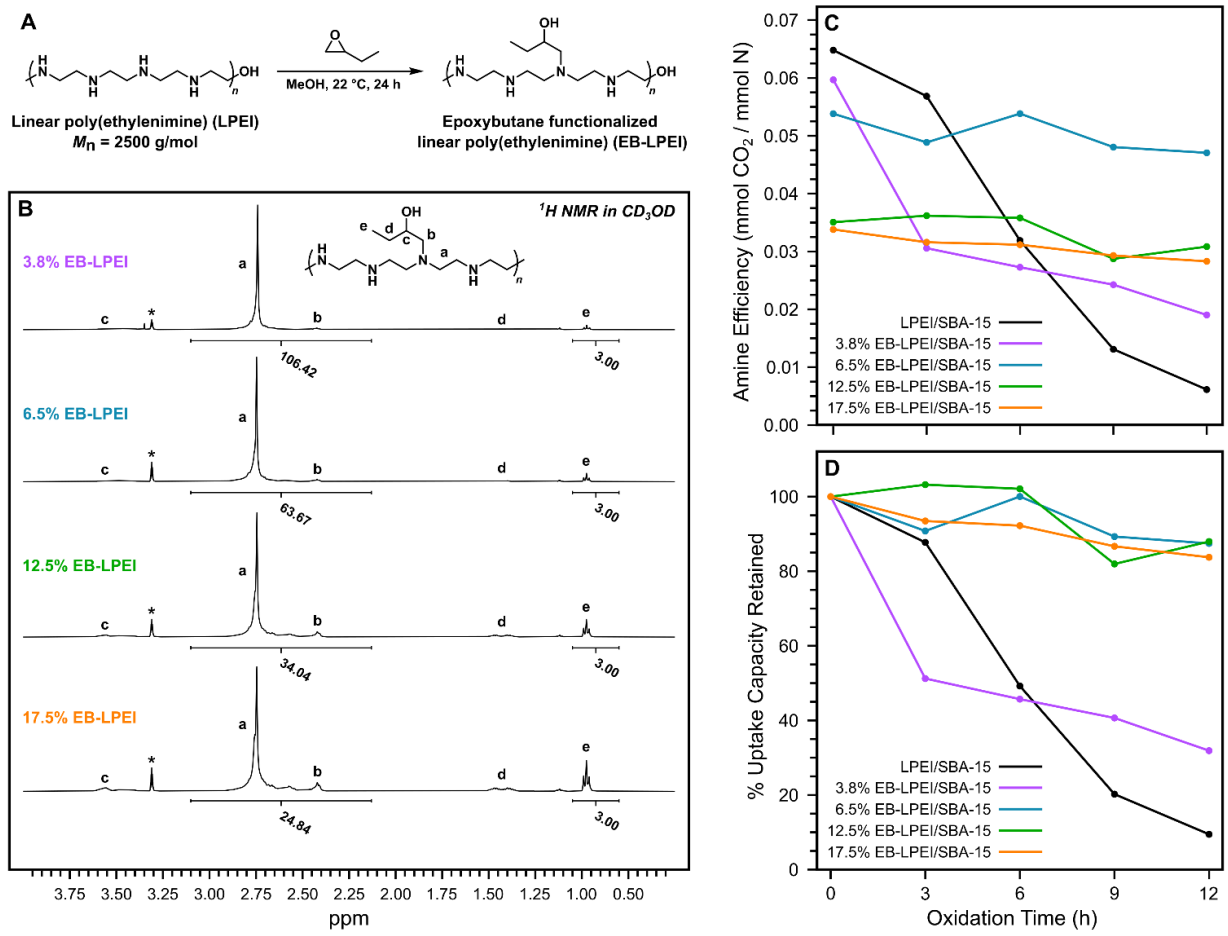

Figure 2. (A) Synthesis of hydroxyl-functionalized linear poly(ethylenimine)s (EB-LPEIs). (B) ^1H NMR spectra of EB-LPEIs in CD_3OD. * denotes residual solvent signal. (C) CO_2 uptake capacity amine efficiencies (in mmol CO_2 per mmol N) as a function of oxidation time for LPEI/SBA-15 and EB-LPEI/SBA-15. Uptake values were determined by thermogravimetric analysis using dry 410 ppm CO_2 in N_2. (D) Percentages of retained CO_2 uptake capacities (relative to pristine adsorbents) as a function of oxidation time for LPEI/SBA-15 and EB-LPEI/SBA-15. All composites with SBA-15 were prepared at 40 wt% polymer.

While the materials had negligible difference in initial uptake rates, polymers with higher extents of functionalization (12.5% and 17.5%) ultimately reached their equilibrium uptake capacities faster than LPEI. To determine the impact of hydroxyl functionalization on sorbent stability, a series of accelerated oxidation experiments were performed via TGA, in which sorbents were exposed to a dry 80:20 N_2:O_2 gas mixture at 110 °C for 3 h, 6 h, 9 h, and 12 h. Consistent with literature reports for analogous branched poly(ethylenimine) systems, epoxide functionalization generally increased oxidative stability relative to unfunctionalized LPEI, which lost nearly all of its CO_2 uptake capacity after 12 h of oxidation. While relatively low extents of functionalization (i.e. 6.5% and higher) resulted in at least 80% retention of CO_2 uptake (Figure 2D), 3.8% EB-LPEI experienced a significant loss in uptake, indicating a threshold of hydroxyl content that is necessary to achieve resistance to oxidation. Furthermore, while 3.8% EB-LPEI retained a higher uptake capacity than LPEI after the full 12 h of oxidation, it also showed a faster initial decrease in uptake capacity. It is possible that at sufficiently low extents of functionalization, the hydroxyl groups promote radical formation and/or propagation, similar to the recently reported observations of water vapor[7] and low CO_2 levels[30] accelerating oxidative degradation in BPEI. Given that increased functionalization extents resulted in progressively lower CO_2 uptake capacities as previously mentioned, 6.5% EB-LPEI emerged as the optimal balance of stability and uptake performance within the series of materials. A couple of different mechanisms were envisioned to be responsible for the observed improved oxidative stability upon hydroxyl functionalization. The increased hydrogen bonding strength between hydroxyls and amines could mitigate propogation of degradation mechanisms by reducing polymer mobility.[7,27,31] Alternatively, the hydroxyl side chains could undergo oxidation at a faster rate than the aminopolymer backbone, thereby acting as sacrifical moieties initially (i.e. under the time lengths investigated) and contributing diminishing effectiveness over longer time frames. To evaluate the integrity of the hydroxyl side chains over the course of oxidation, polymer samples were extracted from oxidized sorbents using D_2O and analyzed via ^{1}H NMR (Figure 3).

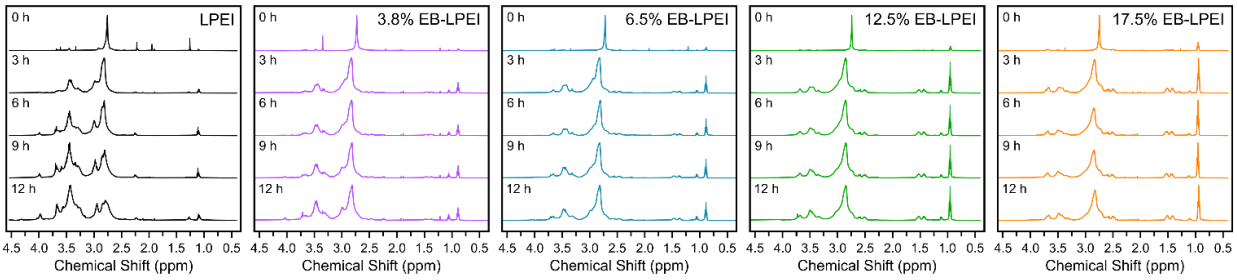

Figure 3. ^{1}H NMR spectra of LPEI and EB-LPEIs at each time point generated in accelerated oxidation studies. For each time point (including 0 h), polymer samples were extracted from the SBA-15 support via sonication in D_2O, and the suspensions were then filtered using 0.22 μm PES syringe filters.

As anticipated, the NMR spectra of LPEI showed a steady decrease in the relative intensity of the original LPEI backbone –CH_2– peak around 2.8 ppm as oxidation time increased. Simultaneously, a broad peak centered around 3.5 ppm steadily grew in intensity, corresponding to oxidized polymer material likely containing functional groups such as amides and imines as has

been reported for other poly(ethylenimine) materials.[5–7,10,11] Additional signals around 8 ppm also became more prevalent over the course of oxidation (Figure S12), consistent with these types of functionalities (i.e. C=N or C=O containing species), and was further supported by FT-IR analysis, in which a peak at 1660 cm^{-1} emerged over the course of the oxidation (Figure S17). At progressively higher functionalization extents, the emergence of signals attributed to oxidized species (around 3.5 ppm and 8 ppm) continued to become less prevalent (see Figures S13-S16 for full spectra), consistent with a slower rate of degradation and higher retained uptake capacities compared to LPEI and 3.8% EB-LPEI. Moreover, the peaks corresponding to the hydroxyl-containing side chains remained relatively unchanged, suggesting they are indeed contributing to a polymer system that is overall more resistant to oxidation.

Differential Scanning Calorimetry

The impact of hydroxyl functionalization on the physical properties of LPEI was characterized using differential scanning calorimetry (DSC).[32] As shown in Figure 4A, which highlights the DSC traces for the series of SBA-15 supported LPEIs, LPEI in SBA-15 has a glass transition temperature (T_g) around -39 °C under confinement, and introduction of hydroxyl functionalities gradually increases the polymer's T_g, with 17.5% EB-LPEI in SBA-15 having a T_g of around -30 °C. This trend is consistent with previously reported data for BPEI,[27] although prior investigations used materials with higher hydroxyl contents and solely looked at the properties of the bulk polymers and therefore could not capture any potential confinement effects. Interestingly, for LPEI/SBA-15 and 3.8% EB-LPEI/SBA-15, a second, weaker transition was observed around 20-25 °C. This can likely be attributed to melting of residual semi-crystalline or crystalline regimes;[33] this phenomenon is observed in the bulk LPEI, 3.8% EB-LPEI, and 6.5% EB-LPEI materials (Figure S18), but is suppressed upon confinement. Notably, the intensity of these more crystalline/ordered thermal transitions in the bulk polymers steadily decreased from LPEI to 6.5% EB-LPEI, and were completely absent in both 12.5% EB-LPEI and 17.5% EB-LPEI, indicating that any crystalline nature of LPEI had been largely eliminated at these higher extents of functionalization.

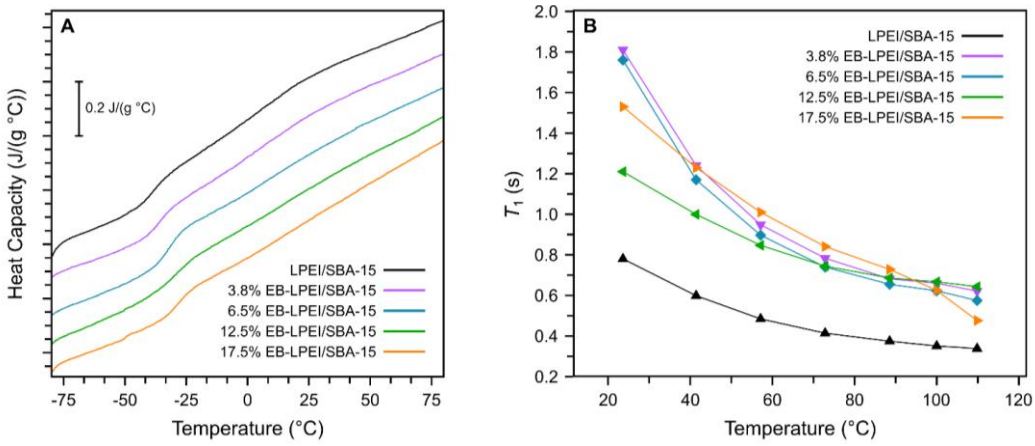

Figure 4. (A) Differential scanning calorimetry (DSC) of polymer/SBA-15 composites. Samples were measured using a heating rate of 20 °C/min. (B) T_1 relaxation constants for polymer/SBA-15 composites as a function of temperature.

Solid-State NMR Relaxometry

Further analysis of the impact of hydroxyl functionalization on the physical properties of LPEI was accomplished by a series of NMR relaxometry experiments, which have garnered increasing attention as a non-destructive method to evaluate polymer mobility and sorbent integrity.[34–37] The series of polymer/SBA-15 composites was evaluated over a range of temperatures, with an emphasis on including higher temperatures (i.e. up to 110 °C) to better understand the physical properties of the confined polymers under DAC relevant conditions.

Figure 4B shows the ^{1}H spin-lattice relaxation (T_1) times for the series of composites. T_1 is sensitive to fast motions at the Larmor frequency and is expected to increase as the molecular motion decreases, corresponding to a lower polymer mobility. Over the measured range of 25–110 °C, T_1 decreases for all materials, indicating increased polymer mobility at higher temperatures as expected. Notably, however, there is a distinct difference between the LPEI and all hydroxyl-functionalized materials, with the former having a markedly lower T_1 value at all measured temperatures. For example, in the 100–110 °C temperature range, the T_1 values for LPEI are around 0.3 s, while those of the EB-LPEI series range from 0.6–0.7 s, with the exception of 17.5% EB-LPEI at 110 °C. ^{1}H T_1 is influenced by proton driven spin diffusion which has an averaging effect across dynamical heterogeneities in the sample resulting in single, averaged T_1 value for the whole spin system. ^{1}H transverse relaxation (T_2) is also sensitive to molecular motion via changes to dipolar couplings and is not influenced by spin diffusion enabling the relaxation for specific chemical environments to be more easily observed. There are two pools of proton spins, those associated with surface hydroxyls and those within LPEI; the latter have further dynamical heterogeneity as regions of the aminopolymer chain is more strongly interacting with the surface silanols.[35] The dynamical heterogeneity for each chemical environment is revealed using T_2 relaxation ordered spectroscopy (ROSY) which correlates chemical shift to T_2 relaxation distributions (Figure S20). The relaxation distributions for the chemical shift regions for the LPEI backbone and epoxide functionals are shown in Figure S21. Relaxation from silanols is also captured in these relaxation curves because of overlapping chemical shifts but is relatively small in intensity due to limited silanols relative to LPEI in the sample. In the LPEI region, there is a relaxation peak that trends towards lower T_2 values as the degree of hydroxyl functionalization increases, indicating lower mobility of the parts of the LPEI chain. Within the EB region the relaxation distributions display more variance across samples, however the relaxations trend towards lower T_2 values after 6.5% hydroxyl functionalization. This indicates that the mobility of the hydroxyl groups decreases from greater hydrogen bonding interactions across hydroxyl functional groups, as supported by the simulations discussed in the following section. Consistent with the DSC characterization, the relaxation results indicate that the average polymer mobility of the EB-LPEI materials is lower than LPEI even at elevated temperatures, which, when combined with the observed oxidation rates, further supports the hypothesis that polymer mobility is a driving factor in defining material stability.

Molecular Simulations of LPEI Chain Dynamics

To further elucidate the impact of hydroxyl functionalities on the mobility of LPEI, molecular dynamics simulations were conducted using a machine learning interatomic potential trained on extensive ab initio molecular dynamics trajectories through an active learning scheme. Calculations were performed on condensed-phase linear poly(ethylenimine)s with either 0%, 5%, 10%, or 15% of the repeat units having a hydroxyl-containing side chain to cover a range similar to the experimentally investigated polymer series. Additionally, the temperature for simulations was set to 100 °C in an effort to best capture chain dynamics at the elevated temperatures typically involved with sorbent regeneration.

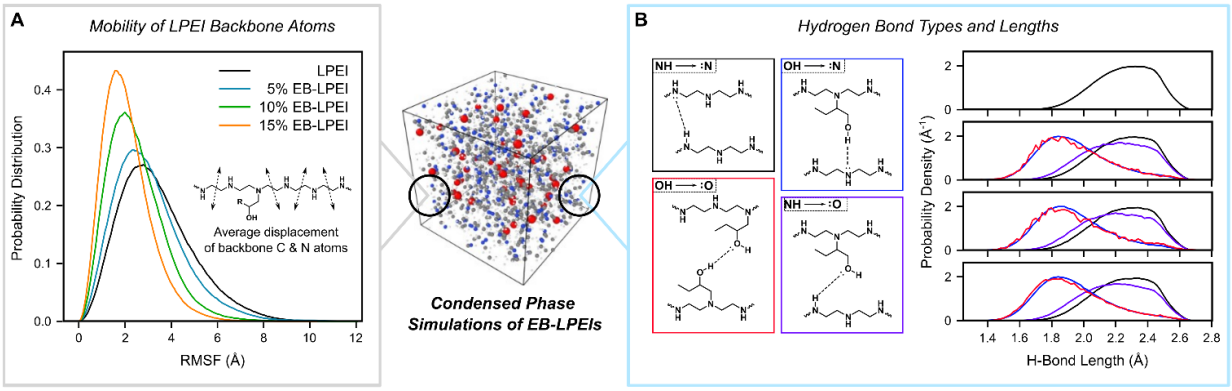

Figure 5. (A) Condensed phase molecular simulations of chain dynamics hydroxyl-functionalized linear poly(ethylenimine)s at 100 °C. Probability distributions for root mean square fluctuations (RMSF) of backbone atoms (C and N) in LPEI, 5% EB-LPEI, 10% EB-LPEI, and 15% EB-LPEI. (B) Probability densities of the H-bond lengths for four different hydrogen bonding modes (donor:acceptor; N:N (black), O:N (blue), O:O (red), N:O (purple)) in LPEI, 5% EB-LPEI, 10% EB-LPEI, and 15% EB-LPEI. H-bond lengths were calculated as the distance between the involved heteroatoms.

Figure 5A shows the probability distributions for the root mean square fluctuations (RMSF) of the polymer backbones, which were defined as the backbone carbon and nitrogen atoms (i.e. not including the carbon or oxygen atoms in the hydroxyl side chains). While LPEI had a distribution centered around approximately 2.5-3 Å, increasing hydroxyl content gradually shifted the center of the distributions to below 2 Å and resulted in decreased distribution widths. These changes indicate that, consistent with experimental DSC and NMR data, increasing hydroxyl content acts to decrease the mobility of LPEI, which is hypothesized to be a prominent factor in the increased oxidative stability of these materials.

In addition to the backbone mobilities, the hydrogen bonding networks within these condensed phase polymer systems were characterized (Figure 5B). Specifically, the four different types of hydrogen bonding modes were investigated: nitrogen donor to nitrogen acceptor (black), oxygen donor to nitrogen acceptor (blue), oxygen donor to oxygen accepter (red), and nitrogen donor to oxygen acceptor (purple). Overall, there is a clear difference in the average hydrogen bond length (defined as the distance between the involved heteroatoms) which is defined by the nature of the hydrogen bond donor. More specifically, modes in which oxygen acted as the donor showed probability densities centered around 1.8 Å, around 0.5 Å lower than the

centers of the distributions for modes in which nitrogen acted as the donor. The shorter bond lengths of these oxygen-containing hydrogen bonds, indicative of their greater bond strength, provide a clear structural basis for the observed decrease in backbone mobility with increasing hydroxyl content, and their persistence at the elevated temperatures used in the simulations also supports their effectiveness at the temperatures typically used in adsorbent regeneration.

Conclusion

In this work, hydroxyl functionalization of linear poly(ethylenimine) is demonstrated to be a viable strategy towards improving oxidative stability, consistent with observed behavior for branched poly(ethylenimine) based materials. Characterization of the chemical structures after accelerated oxidation experiments indicates that the hydroxyl side chains remain stable, while a combination of DSC, NMR, and molecular simulations highlight the role of hydroxyl groups in decreasing polymer mobility, all of which further supports the hypothesis that mobility is a key factor in defining oxidative stability. Overall, this work provides a deeper understanding of the role of hydroxyl functionalization of aminopolymers by expanding on the scope of materials reported to-date.

Experimental Section

Materials and Methods

Chemicals for synthesis were obtained from Sigma Aldrich and used directly without further purification. The synthesis of SBA-15 was carried out via a previously reported procedure.[38] ^{1}H and ^{13}C NMR spectra were collected at 300 K on a Bruker AVANCE III HD 500 MHz spectrometer with a Bruker cryoprobe operating at 500 MHz for ^{1}H and 126 MHz for ^{13}C. NMR spectra are referenced to residual solvents signals as follows: 3.31 ppm for ^{1}H in CD_3OD, 4.79 ppm for ^{1}H in D_2O, and 49.0 ppm for ^{13}C in CD_3OD. Infrared spectra were measured under ambient conditions on a Bruker Alpha FTIR spectrometer with a zinc selenide ATR crystal. Scans were carried out from 400 to 4000 cm^{-1} with a step size of 1 cm^{-1}.

Synthesis of EB-LPEIs

A 100 mL Schlenk flask was charged with linear poly(ethylenimine) (1.00 g, 0.4 mmol polymer, 23.2 mmol repeat unit, M_n = 2500 g/mol) and vacuum backfilled 3 times with argon. 10 mL anhydrous methanol was added, and after stirring for 15 minutes, 1,2-epoxybutane (3.8% EB-LPEI: 0.10 mL, 1.15 mmol; 6.5% EB-LPEI: 0.20 mL, 2.30 mmol; 12.5% EB-LPEI: 0.40 mL, 4.60 mmol; 17.5% EB-LPEI: 0.60 mL, 6.90 mmol) was added dropwise. The reaction mixture was stirred for 24 h at 22 °C. The methanol was then removed under high vacuum for 48 h at 22 °C and then 5 h at 50 °C, yielding a viscous, slightly yellow oil.

^{1}H NMR (500 MHz, CD_3OD) δ 3.64 – 3.34 (m, 1H), 3.00 – 2.51 (m), 2.49 – 2.36 (m, 2H), 1.54 – 1.32 (m, 2H), 0.98 (t, J = 7.5 Hz, 3H).

^{13}C NMR (126 MHz, CD_3OD) δ 79.5, 71.7, 62.2, 55.4, 49.7, 48.2, 29.0, 10.5.

LPEIs/SBA-15 Composite Preparation

The 40 wt% composites ((EB-)LPEI/SBA-15) were prepared by wet impregnation of (EB-)LPEI into SBA-15. SBA-15 was dried under vacuum at 100 °C for 24 h prior to use. Two mixtures were prepared: one containing 300 mg SBA-15 dispersed in 6 mL methanol via sonication and subsequent stirring at room temperature; a second containing 200 mg (EB-)LPEI dissolved in 6 mL methanol, stirred under argon at room temperature. After stirring for 1 hour, the (EB-)LPEI solution was added to the SBA-15 suspension and stirred overnight at room temperature. The methanol was then removed via rotary evaporation, and the solid was dried under high vacuum at 50 °C overnight, before being backfilled with argon and transferred to an argon filled glovebox for storage. The polymer loading was confirmed via thermogravimetric analysis.

Gravimetric CO_2 Adsorption

CO_2 uptake experiments were performed using a SDT 650 Simultaneous Thermal Analyzer (TA Instruments). A 10-15 mg sample of composite was held under N_2 atmosphere with mass flow 100 mL/min, the temperature was increased at 10 °C/min to 110 °C and held for 2 h to desorb atmospheric CO_2 and water. The temperature was decreased at 10 °C/min to 30 °C and held for 3 h to allow the sample mass to equilibrate. The inlet gas was switched to a 401.4 ppm CO_2 balance N_2 gas mixture with mass flow 100 mL/min, and the sample was allowed to adsorb CO_2 for 18 hours at 30 °C.

Accelerated Oxidative Treatment

Samples were oxidized using a SDT 650 Simultaneous Thermal Analyzer (TA Instruments). A 10-15 mg sample of composite was held under N_2 atmosphere with mass flow 100 mL/min, the temperature was increased at 10 °C/min to 110 °C and held for 2 h to desorb atmospheric CO_2 and water. The inlet gas was switched to ultra zero air with mass flow 100 mL/min and the sample was allowed to oxidize at 110 °C for a specified amount of time before switching back to N_2. The temperature was decreased at 10 °C/min to 30 °C before exposing the sample to atmosphere for further analysis.

^{1}H NMR Relaxometry

Composite materials were dried in 50 mL round bottom flasks under vacuum at 50 °C overnight to remove any trace water or volatiles. After transferring into a glovebox, the composites were packed into 1.6 mm NMR rotors. T_1 relaxometry experiments were conducted using a 400 MHz Bruker Neo NMR spectrometer equipped with a Bruker Smartcooler BCU II variable temperature controller. All measurements were collected spinning at 25 kHz and with a recycle delay of 6 s. ^{1}H T_1 and T_2 relaxation measurements used a 2.5 µs and 5 µs pulse for the 90° and 180° pulses, respectively, corresponding to a RF strength of 100 kHz. T_1 values were determined via an inversion recovery experiment, using 16 increments from 10 ms to 15 s. T_2 values were collected via a CPMG (Carr-Purcell-Meiboom-Gill) pulse sequence using an echo time of 170 µs. Analysis of the T_2 curves could not be simply fit with a mono- or biexponential function due to the heterogenous nature of the composite sample. Rather multiexponential analysis was used by performing a regularized inversion of the data using a Python script adapted from Afrough et al.[39] and analyzed as a ROSY plot to correlate chemical shift to the relaxation distributions.

Experiments were collected over a range of temperatures from room temperature to 110 °C, where the temperature of the sample was calibrated externally using the chemical shift temperature dependence of lead nitrate.[40]

Ab Initio Molecular Dynamics

NVT ab initio molecular dynamics (AIMD) simulations were conducted for conformational sampling of flexible LPEI structures and to provide data for the training of machine learning interatomic potential using the Vienna ab initio simulation package (VASP), version 5.4.4.[41] The simulations employed the projector augmented wave method for core-valence interactions[42] and utilized the Perdew–Burke–Ernzerhof (PBE) generalized gradient approximation for exchange-correlation energy.[43] The energy cutoff for the plane-wave basis set was established at 400 eV, and the Brillouin zone was sampled using only the Γ-point. Self-consistent-field electronic energies were converged to within 10^{-4} eV. A time step of 1 fs was implemented, and the Nosé-Hoover thermostat was applied to maintain the temperature at 473 K. The simulations utilized cubic cells containing eight LPEI molecules ($C_{12}H_{31}N_7$), with the cell dimensions adjusted to achieve a BPEI density of 1.05 g/mL. For the simulation cell containing EB-functionalized LPEI, one pendant functional group was attached to a randomly selected secondary amine site on each LPEI molecule.

Random Structure Generation

The initial simulation cells for machine learning molecular dynamics simulations were created by randomly placing 16 LPEI molecules ($C_{30}H_{78}N_{16}$) within a three-dimensional periodic cubic supercell using a Monte Carlo method.[44] A low initial density of 0.1 g/cm³ was selected to prevent overlap between adjacent molecules and to allow for the later addition of pendant hydroxyl groups. Structures with 5%, 10%, and 15% functionalization were generated by adding the appropriate number of functional groups to randomly selected secondary amine sites. All initial supercells were then compressed to near-equilibrium density (approximately 1 g/cm³) using 100 ps NPT simulations with the Andersen thermostat and barostat,[45] which maintain the cubic cell shape during volume changes. Interatomic interactions were modeled using the COMPASS class II force field, which has been extensively validated for condensed systems like polymer melts and organic liquids, including amine solvent systems.[46,47] Long-range Coulomb interactions were addressed using the Ewald summation technique.[48,49] The resulting structures from this process served as starting points for further equilibration with machine-learned (ML) force fields, as detailed below.

Machine Learning Accelerated Molecular Dynamics

Molecular dynamics simulations of pure and epoxy-functionalized LPEI were performed with a machine learning interatomic potential (MLIP) trained on the PBE density functional[43] with the D3 dispersion correction.[50] The MLIP architecture followed the MACE model,[51] and its training data consisted of 936 configurations of systems containing 8 LPEI polymers (with 0 or 14 % O/N epoxy functionalization) per periodically repeating cell. The MACE training data were collected through reinforcement learning. The exploration of new data was performed through molecular dynamics simulations at 400 K and 1 bar, and only atomic configurations exceeding 0.1 eV/A maximum error in forces were re-evaluated with DFT and appended to the existing training data. The production molecular simulations were done on systems with approximately 2000 atoms, with temperature

and pressure controlled at 373 K and 1 bar by a Berendsen thermostat and barostat with time constants of 0.1 and 1 ps, respectively. All molecular simulations were performed with the ASE code,[52] while all DFT calculations used the Quantum-ESPRESSO package.[53] DFT calculations were performed with a plane-wave cutoff of 110 Ry and Troullier-Martins norm-conserving pseudopotentials.[54]

Acknowledgements

This work was supported by the U.S. Department of Energy, Office of Science, Basic Energy Sciences, Materials Sciences and Engineering Division. Work at Lawrence Livermore National Laboratory was performed under the auspices of the U.S. Department of Energy under Contract DE-AC52-07NA27344. Computational resources were provided under the LLNL Grand Challenge Program This research used computational resources from the LLNL Computing Grand Challenge Programm and from the National Energy Research Scientific Computing Center (NERSC), a U.S. Department of Energy Office of Science User Facility located at Lawrence Berkeley National Laboratory, operated under Contract No. DE-AC02-05CH11231 using NERSC award BES-ERCAP0023097. IM release number: LLNL-JRNL-871023-DRAFT.

Keywords: aminopolymer degradation • carbon dioxide removal • carbon capture • amine-based adsorbent • material lifetime

References

1 X. Xu, C. Song, J. M. Andresen, B. G. Miller and A. W. Scaroni, *Energy Fuels*, 2002, **16**, 1463–1469.

2 S. A. Didas, S. Choi, W. Chaikittisilp and C. W. Jones, *Acc. Chem. Res.*, 2015, **48**, 2680–2687.

3 S. Chowdhury, Y. Kumar, S. Shrivastava, S. K. Patel and J. S. Sangwai, *Energy Fuels*, 2023, **37**, 10733–10757.

4 X. Zhu, W. Xie, J. Wu, Y. Miao, C. Xiang, C. Chen, B. Ge, Z. Gan, F. Yang, M. Zhang, D. O'Hare, J. Li, T. Ge and R. Wang, *Chem. Soc. Rev.*, 2022, **51**, 6574–6651.

5 M. J. Lashaki, S. Khiavi and A. Sayari, *Chem. Soc. Rev.*, 2019, **48**, 3320–3405.

6 Y. A. Guta, J. Carneiro, S. Li, G. Innocenti, S. H. Pang, M. A. Sakwa-Novak, C. Sievers and C. W. Jones, *ACS Appl. Mater. Interfaces*, 2023, **15**, 46790–46802.

7 J. S. A. Carneiro, G. Innocenti, H. J. Moon, Y. Guta, L. Proaño, C. Sievers, M. A. Sakwa-Novak, E. W. Ping and C. W. Jones, *Angew. Chem. Int. Ed.*, 2023, **62**, e202302887.

8 J. Racicot, S. Li, A. Clabaugh, C. Hertz, S. A. Akhade, E. W. Ping, S. H. Pang and M. A. Sakwa-Novak, *J. Phys. Chem. C*, 2022, **126**, 8807–8816.

9 I. Nezam, J. Xie, K. W. Golub, J. Carneiro, K. Olsen, E. W. Ping, C. W. Jones and M. A. Sakwa-Novak, *ACS Sustainable Chem. Eng.*, 2021, **9**, 8477–8486.

10 A. Ahmadalinezhad and A. Sayari, *Phys. Chem. Chem. Phys.*, 2014, **16**, 1529–1535.

11 A. Sayari, A. Heydari-Gorji and Y. Yang, *J. Am. Chem. Soc.*, 2012, **134**, 13834–13842.

12 A. Heydari-Gorji and A. Sayari, *Ind. Eng. Chem. Res.*, 2012, **51**, 6887–6894.

13 S. Bali, T. T. Chen, W. Chaikittisilp and C. W. Jones, *Energy Fuels*, 2013, **27**, 1547–1554.

14 P. Bollini, S. Choi, J. H. Drese and C. W. Jones, *Energy Fuels*, 2011, **25**, 2416–2425.

15 S. A. Didas, R. Zhu, N. A. Brunelli, D. S. Sholl and C. W. Jones, *J. Phys. Chem. C*, 2014, **118**, 12302–12311.

16 W. Choi, K. Min, C. Kim, Y. S. Ko, J. W. Jeon, H. Seo, Y.-K. Park and M. Choi, *Nat. Commun.*, 2016, **7**, 12640.

17 K. Min, W. Choi, C. Kim and M. Choi, *Nat. Commun.*, 2018, **9**, 726.

18 C. Kim, Y. Ha and M. Choi, *Acc. Chem. Res.*, 2023, **56**, 2887–2897.

19 K. Min, W. Choi, C. Kim and M. Choi, *ACS Appl. Mater. Interfaces*, 2018, **10**, 23825–23833.

20 W. Choi, J. Park, C. Kim and M. Choi, *Chem. Eng. J.*, 2021, **408**, 127289.

21 H. E. Holmes, S. Banerjee, A. Vallace, R. P. Lively, C. W. Jones and M. J. Realff, *Energy Environ. Sci.*, 2024, **17**, 4544–4559.

22 S. Park, J. Kim, Y.-J. Won, C. Kim, M. Choi, W. Jung, K. S. Lee, J.-G. Na, S.-H. Cho, S. Y. Lee and J. S. Lee, *Ind. Eng. Chem. Res.*, 2018, **57**, 13923–13931.

23 J. M. Kolle and A. Sayari, *Ind. Eng. Chem. Res.*, 2020, **59**, 6944–6950.

24 M. Guo, S. Liang, J. Liu, J. Jin and J. Mi, *ACS Sustainable Chem. Eng.*, 2020, **8**, 3853–3864.

25 S. Park, K. Choi, H. J. Yu, Y.-J. Won, C. Kim, M. Choi, S.-H. Cho, J.-H. Lee, S. Y. Lee and J. S. Lee, *Ind. Eng. Chem. Res.*, 2018, **57**, 4632–4639.

26 A. Goeppert, H. Zhang, R. Sen, H. Dang and G. K. S. Prakash, *ChemSusChem*, 2019, **12**, 1712–1723.

27 S. Li, M. F. Calegari Andrade, A. J. Varni, G. A. Russell-Parks, W. A. Braunecker, E. Hunter-Sellars, M. A. T. Marple and S. H. Pang, *Chemical Communications*, 2023, **59**, 10737–10740.

28 W. Chaikittisilp, H.-J. Kim and C. W. Jones, *Energy Fuels*, 2011, **25**, 5528–5537.

29 S. H. Pang, R. P. Lively and C. W. Jones, *ChemSusChem*, 2018, **11**, 2628–2637.

30 S. Li, Y. Guta, M. F. Calegari Andrade, E. Hunter-Sellars, A. Maiti, A. J. Varni, P. Tang, C. Sievers, S. H. Pang and C. W. Jones, *J. Am. Chem. Soc.*, 2024, **146**, 28201–28213.

31 S. Li, M. R. Cerón, H. V. Eshelman, A. J. Varni, A. Maiti, S. Akhade and S. H. Pang, *ChemSusChem*, 2023, **16**, e202201908.

32 H. Correll, N. Leick, R. E. Mow, G. A. Russell-Parks, S. H. Pang, T. Gennett and W. A. Braunecker, *J. Phys. Chem. C*, 2022, **126**, 10419–10428.

33 W. Buijs, *Ind. Eng. Chem. Res.*, 2021, **60**, 11309–11316.

34 E. Hunter-Sellars, J. D. Kerr, H. V. Eshelman, Z. A. Pollard, A. J. Varni, M. A. Sakwa-Novak, M. A. T. Marple and S. H. Pang, *Macromolecular Chemistry and Physics*, 2024, **225**, 2400023.

35 H. J. Moon, R.-S. Sekiya and C. W. Jones, *J. Phys. Chem. C*, 2023, **127**, 11652–11665.

36 G. A. Russell-Parks, N. Leick, M. A. T. Marple, N. A. Strange, B. G. Trewyn, S. H. Pang and W. A. Braunecker, *J. Phys. Chem. C*, 2023, **127**, 15363–15374.

37 R. Fonseca, R. Vieira, M. Sardo, I. Marin-Montesinos and L. Mafra, *J. Phys. Chem. C*, 2022, **126**, 12582–12591.

38 G. S. Foo, J. J. Lee, C.-H. Chen, S. E. Hayes, C. Sievers and C. W. Jones, *ChemSusChem*, 2017, **10**, 266–276.

39 A. Afrough, R. Mokhtari and K. L. Feilberg, *Magnetic Resonance in Chemistry*, 2024, **62**, 698–711.

40 O. Dmitrenko, S. Bai, P. A. Beckmann, S. van Bramer, A. J. Vega and C. Dybowski, *J. Phys. Chem. A*, 2008, **112**, 3046–3052.

41 G. Kresse and J. Furthmüller, *Phys. Rev. B*, 1996, **54**, 11169–11186.

42 P. E. Blöchl, *Phys. Rev. B*, 1994, **50**, 17953–17979.

43 J. P. Perdew, K. Burke and M. Ernzerhof, *Phys. Rev. Lett.*, 1996, **77**, 3865–3868.

44 D. N. Theodorou and U. W. Suter, *Macromolecules*, 1986, **19**, 139–154.

45 H. C. Andersen, *The Journal of Chemical Physics*, 1980, **72**, 2384–2393.

46 A. Maiti, W. L. Bourcier and R. D. Aines, *Chemical Physics Letters*, 2011, **509**, 25–28.

47 M. Sharif, T. Han, T. Wang, X. Shi, M. Fang, D. Shuming, R. Meng and X. Gao, *Chemical Engineering Research and Design*, 2024, **204**, 524–535.

48 P. P. Ewald, *Annalen der Physik*, 1921, **369**, 253–287.

49 M. P. Tosi, in *Solid State Physics*, eds. F. Seitz and D. Turnbull, Academic Press, 1964, vol. 16, pp. 1–120.

50 S. Grimme, J. Antony, S. Ehrlich and H. Krieg, *The Journal of Chemical Physics*, 2010, **132**, 154104.

51 I. Batatia, D. P. Kovacs, G. Simm, C. Ortner and G. Csanyi, 2022, vol. 35, pp. 11423–11436.

52 A. H. Larsen, J. J. Mortensen, J. Blomqvist, I. E. Castelli, R. Christensen, M. Dułak, J. Friis, M. N. Groves, B. Hammer, C. Hargus, E. D. Hermes, P. C. Jennings, P. B. Jensen, J. Kermode, J. R. Kitchin, E. L. Kolsbjerg, J. Kubal, K. Kaasbjerg, S. Lysgaard, J. B. Maronsson, T. Maxson, T. Olsen, L. Pastewka, A. Peterson, C. Rostgaard, J. Schiøtz, O. Schütt, M. Strange, K. S. Thygesen, T. Vegge, L. Vilhelmsen, M. Walter, Z. Zeng and K. W. Jacobsen, *J. Phys.: Condens. Matter*, 2017, **29**, 273002.

53 P. Giannozzi, O. Andreussi, T. Brumme, O. Bunau, M. B. Nardelli, M. Calandra, R. Car, C. Cavazzoni, D. Ceresoli, M. Cococcioni, N. Colonna, I. Carnimeo, A. D. Corso, S. de Gironcoli, P. Delugas, R. A. DiStasio, A. Ferretti, A. Floris, G. Fratesi, G. Fugallo, R. Gebauer, U. Gerstmann, F. Giustino, T. Gorni, J. Jia, M. Kawamura, H.-Y. Ko, A. Kokalj, E. Küçükbenli, M. Lazzeri, M. Marsili, N. Marzari, F. Mauri, N. L. Nguyen, H.-V. Nguyen, A. Otero-de-la-Roza, L. Paulatto, S. Poncé, D. Rocca, R. Sabatini, B. Santra, M. Schlipf, A. P. Seitsonen, A. Smogunov, I. Timrov, T. Thonhauser, P. Umari, N. Vast, X. Wu and S. Baroni, *J. Phys.: Condens. Matter*, 2017, **29**, 465901.

54 N. Troullier and J. L. Martins, *Phys. Rev. B*, 1991, **43**, 1993–2006.